applied optics

Integrated refractive index sensor using silicon slot waveguides

Ka Li, Xue Feng,* Kaiyu Cui, Wei Zhang, Fang Liu, and Yidong Huang

Department of Electronic Engineering, Tsinghua National Laboratory for Information Science and Technology, Tsinghua University, Beijing 100084, China
**Corresponding author: x-feng@tsinghua.edu.cn*

Received 9 January 2017; revised 28 February 2017; accepted 9 March 2017; posted 10 March 2017 (Doc. ID 284252); published 6 April 2017

We propose an integrated refractive index (RI) sensor based on evanescent field absorption (EFA) within a silicon slot waveguide, where the RI variation is translated into a varied attenuation coefficient and eventually the output power at the end of the waveguide. To demonstrate the operating principle of such a RI-EFA sensor, a specific structure is designed and discussed with numerical simulations. The calculated results indicate that the detection limit of our proposed RI-EFA sensor could be as good as $\sim 10^{-8}$ RIU for homogeneous sensing and $\sim 10^{-7}$ RIU for surface sensing with optimized structural parameters at a wavelength of 1064 nm. Since only a straight slot waveguide and optical power detection are required for our proposed sensor, we believe that it is promising to achieve an integrated and portable sensor on a single chip.

OCIS codes: (130.6010) Sensors; (300.1030) Absorption; (130.3120) Integrated optics devices; (280.1415) Biological sensing and sensors.

https://doi.org/10.1364/AO.56.003096

1. INTRODUCTION

Optical biosensors have been an active research area for a long time since they can be applied in various fields, such as medical diagnostics, food safety, and environment monitoring [1–3]. Generally speaking, biosensors can be divided into two categories, according to the detection technique. One is labeling-based biosensors, such as fluorescence-based biosensors [4], and the other is label-free biosensors [5,6]. For fluorescence-based biosensors, the target molecules are required to be labeled while the label-free biosensors are not. Hence, label-free biosensors are more flexible and suitable for the real-time detection. Furthermore, both sensing schemes can be implemented by integrated planar waveguides [7]. Thus, combined with complementary metal-oxide semiconductor (CMOS) technologies and silicon-on-insulator (SOI) substrates, both miniaturizing the sensors and integration with electronics on the same chip are possible to realize so-called lab-on-a-chip [8]. As we know, the traditional strip or rib waveguides are widely adopted as biosensors for their high refractive index contrast and low transmission loss [9,10]. However, in such waveguides, the light is strongly confined in the high-refractive-index area (silicon region) so that the overlap between light and the sensing material is weak. Thus, the sensitivity of a biosensor based on traditional waveguides is limited. Fortunately, it would be improved while employing a slot waveguide, where the light is guided and strongly confined in the low-refractive-index area (slot region). Thus, the light field distribution is rather sensitive to the refractive index (RI) of the detected material [7,11]. It is worth mentioning that among the different biosensors, the RI biosensors play an important role in biochemical analysis [12]. Furthermore, for these waveguide sensors, there are two sensing mechanisms that are commonly used. One is the homogeneous sensing and the other is surface sensing [13]. However, to interrogate RI variation, a Mach–Zehnder interferometer or a microring resonator is required. On the other hand, another widely employed approach for biosensors is an evanescent field absorption (EFA) sensor, which requires only simple waveguides and optical power detection [14,15]. Unfortunately, conventional EFA sensors are bulky also due to the weak interaction between light and the sensing material [16]. Furthermore, as mentioned, this situation would be greatly changed by introducing a slot waveguide. While the RI of the detected material varies, the light field distribution within the slot waveguide would also be changed. Then, the question is how to interrogate the variation of light field distribution within a slot waveguide.

In this paper, we propose a possible RI sensing mechanism based on the EFA sensor scheme, where the RI variation is translated into a varied attenuation coefficient and eventually the varied output power of the slot waveguide. To demonstrate the proposed sensing mechanism, a specific biochemical sensor is designed and discussed with numerical simulations. The sensor area is considered as a silicon slot waveguide fabricated on a SOI substrate. Both homogeneous sensing and surface sensing

are considered to detect the material in solutions. The operating wavelength is set as ~1 μm, which is within the low absorption band of water but within the high absorption band of silicon. Specifically, the sensor has been optimized in terms of the transverse structural parameters of the slot waveguide at a wavelength of 1064 nm. The output power of the light source, the waveguide length, and additional loss introduced within the fabrication process are also discussed. The obtained results indicate that such a RI-EFA sensor is promising with a RI detection limit up to a magnitude of $\sim 10^{-8}$ RIU for homogeneous sensing and $\sim 10^{-7}$ RIU for surface sensing, while only a slot waveguide and power detection are required. We believe that this work could provide a possible solution for future portable and disposable sensing systems.

2. SYSTEM MODELING

A. Configuration and Sensing Mechanism

In conventional evanescent filed sensors, as mentioned in Section 1, the sensing area is usually an optical fiber or a strip waveguide. The light is always guided in the high-refractive-index section while the refractive index of the sensing area is relatively low. Thus, overlap between the electric field and the sensing material is weak so that the sensitivity of such a traditional evanescent field sensor is limited. However, if the fiber or strip waveguide is substituted by a slot waveguide, where the intensity field distribution can be overlapped with the sensing material much more, a rather high sensitivity for refractive index could be achieved.

Figure 1 shows the schematic of our proposed RI-EFA sensor on a SOI substrate, which consists of a light source, a silicon slot waveguide, and a photodetector (PD). The silicon slot waveguide is considered as a sensing area, in which the sensing solution is assumed to be surrounded by silicon strips on the buried oxide (BOX) layer. Furthermore, there are two sensing mechanisms that are commonly employed for the evanescent field sensors. One is homogeneous sensing and the other is surface sensing. Specifically, the solution is considered as an aqueous solution for both sensing mechanisms. As shown in Fig. 1(a), in the case of homogeneous sensing, the slot waveguide is surrounded with an aqueous solution. The homogeneously distributed analyte in the solution will modify the bulk refractive index of the solution. Meanwhile, for surface sensing, as shown in Fig. 1(b), the sensing material is pretreated as the receptors or

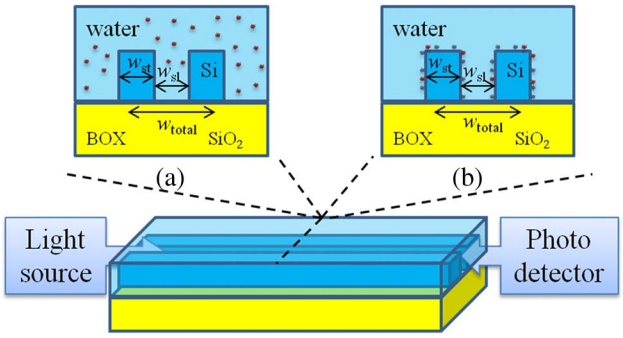

Fig. 1. Schematic of our proposed integrated RI-EFA sensor on a SOI substrate. The inset is the cross section of the slot waveguide.

binding sites, which are adhered to the surface on the silicon strips of the slot waveguide. The refractive index of this surface sensing layer would also change when the receptors or the binding sites bind the specific analyte selectively. For both of the two mechanisms, the refractive index variation of the sensing material would introduce the varied optical confinement factor in the slot waveguide. Consequently, the transmission loss of the slot waveguide would be changed as well as the detected optical power, which can be unambiguously detected by the PD at the end of the waveguide. In this work, both of the homogeneous and surface sensing of the refractive index will be discussed. For more clarity, the system model and some important parameters will be first introduced as follows.

As shown in the Fig. 1, the length and attenuation coefficients of the slot waveguide are denoted as L and α, respectively. First, the coupling loss of the light source/PD to the waveguide is neglected for simplicity; the corresponding impact will be discussed in Section 3. Thus, the incident power of the photodetector ($P_{\mathrm{PD}}^{\mathrm{in}}$) could be simply deduced by assuming the output power of light source as $P_{\mathrm{source}}^{\mathrm{out}}$:

$$P_{\mathrm{PD}}^{\mathrm{in}} = P_{\mathrm{source}}^{\mathrm{out}} e^{-\alpha L}. \tag{1}$$

For an EFA sensor, the refractive index variation of the sensing material could induce a consequential variation of the attenuation coefficient ($\Delta\alpha$) and eventually the received power at PD ($P_{\mathrm{PD}}^{\mathrm{in}}$) [17]. Specifically, when the homogeneous analyte in the cover medium or the surface sensing layer change, the variation of their refractive index (Δn) will introduce the varied light field distribution as well as the attenuation coefficient. Such a mechanism can be quantitatively described as

$$\Delta\alpha = \sum_i \frac{\partial\alpha}{\partial\Gamma_i}\frac{\partial\Gamma_i}{\partial n}\Delta n, \tag{2}$$

where Δn is the refractive index variation of the cover medium or the surface sensing layer and Γ_i is the confinement factor in each region defined as

$$\Gamma_i = \frac{\iint_i |\boldsymbol{E}(x,y)|^2 \mathrm{d}x\mathrm{d}y}{\iint_\infty |\boldsymbol{E}(x,y)|^2 \mathrm{d}x\mathrm{d}y}, \qquad i = s, w, b, \tag{3}$$

where $i = s$, w, b refers to the regions of the silicon strip, the water cladding, and the BOX layer (SiO_2) (as shown in Fig. 1), respectively.

B. Wavelength Selection Criteria

The operating wavelength of our proposed RI-EFA sensor should be carefully selected so that the varied light field distribution could introduce varied transmission loss as much as possible. For this purpose, at the operating wavelength, there should be at least one high-absorption material among the three regions (the silicon strip, the water cladding, and the BOX layer). Thus, large absorption contrast would be achieved to guarantee a highly varied transmission loss with small RI variation. On the other hand, the total transmission loss of the waveguide should be carefully controlled within a certain level to ensure a sufficient signal-to-noise ratio (SNR) at the PD.

Among the silicon strip, the water cladding, and the BOX layer, the silicon dioxide is nearly transparent within near-infrared band (700 nm–2 μm) so that only the silicon or water can serve as the absorption material. Figure 2 shows

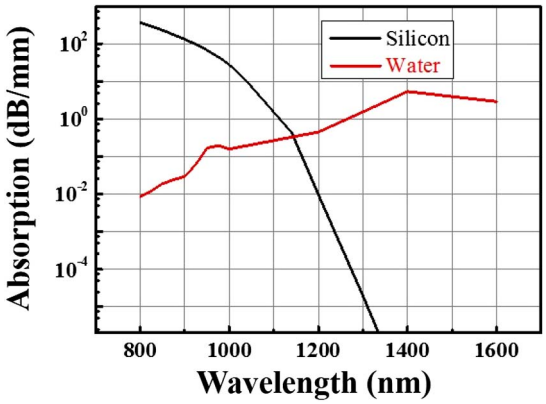

Fig. 2. Near-infrared absorption spectra of silicon and water.

the absorption spectra of both silicon and water within the near-infrared band. It could be seen that either the silicon high absorption band (900–1100 nm) or the telecommunication band (1400–1600 nm) could be optional since there is a significant absorption contrast between silicon and water. However, for biological materials, the sensing wavelength window is about 750–1200 nm since such band is relatively transparent between the high protein absorption (the visible band) and the high water absorption (the telecommunication band) [18]. Furthermore, as mentioned before, the optical intensity inside the slot of the waveguide is very high so that the sensitivity of the sensor would be improved by the good overlapping between light fields and sensing materials. However, the high optical power density inside the slot may cause some damage of the biological samples. Considering this, the water within the slot range is not considered as the high absorption material. Thus, the operating wavelength of our proposed RI-EFA sensor is set as within the silicon high absorption band (900–1100 nm).

For the considered wavelength band of 900–1100 nm, the attenuation coefficient of silicon is 1.5–133 dB/mm while that of the water is less than 0.3 dB/mm. Although such high material absorption would be fatal for light transmission, our previous work has shown that the transmission loss can be significantly reduced by employing a silicon slot waveguide while the interaction between light and the cover material can also be enhanced [19]. Furthermore, within such band, a silicon light source is available [20,21] and the performance of the silicon photodiode is excellent. Thus, an all-silicon system could be massively fabricated with mature CMOS technology, and it is also possible to be integrated with the electronic circuit to control the sensing system or the signal process after the PD. Meanwhile, such a broad range of material absorption also provides some flexibility to engineer both the sensitivity and the transmission property of the slot waveguide.

C. Performance Criteria

To evaluate and compare the performance of an optical sensor, the sensitivity is usually employed as the figure of merit, which is defined as the ratio of the change in the measured optical parameter [13]. For our proposed RI-EFA sensor, the sensitivity (S) is defined as the derivative of the detected power variation by PD about the corresponding refractive index variation and could be expressed by

$$S = \frac{\partial P_{\mathrm{PD}}^{\mathrm{in}}}{\partial n}. \tag{4}$$

According to Section 2.A, the variation of the attenuation coefficient ($\Delta\alpha$) could be induced by the refractive index variation of sensing material (Δn). Thus, with Eqs. (1) and (4), the sensor sensitivity could be expressed by

$$S = \frac{\partial P_{\mathrm{PD}}^{\mathrm{in}}}{\partial n} = P_{\mathrm{source}}^{\mathrm{out}} e^{-\alpha L} \frac{\partial \alpha}{\partial n} L. \tag{5}$$

Furthermore, the variation of RI (Δn) is not so high that the value of $\partial\alpha/\partial n$ is approximated as $\partial\alpha/\partial n \approx \Delta\alpha/\Delta n$ to simplify the calculation. In addition, when the RI of the cover medium or the surface layer change, the attenuation coefficient of the slot waveguide would be from α_0 (the initial loss) to $\alpha = \alpha_0 + \Delta\alpha$ (after the RI change). Furthermore, $\Delta\alpha$ could be treated as a small value compared with the initial loss of α_0 so that Eq. (5) can be approximated as

$$S \approx P_{\mathrm{source}}^{\mathrm{out}} e^{-\alpha_0 L} \frac{\Delta\alpha}{\Delta n} L. \tag{6}$$

In Eq. (6), the terms of $e^{-\alpha_0 L}$ and L refer to the total loss of optical power and the strength of the interaction between light and the sensing material, respectively. Longer L would lead to strong light–material interaction but low SNR in the PD. Thus, there is an optimal value to achieve the highest sensor sensitivity. The optimal waveguide length can be readily solved with $\partial(e^{-\alpha_0 L})L/\partial L = 0$ and the value is $L_{\mathrm{opt}} = 1/\alpha_0$. By substituting it into Eq. (6), the sensor sensitivity with optimal waveguide length could be explicitly expressed as

$$S \approx \frac{P_{\mathrm{source}}^{\mathrm{out}} \cdot \Delta\alpha}{e \cdot \Delta n \cdot \alpha_0}, \tag{7}$$

where e is the base of the natural logarithm. Equation (7) clearly shows that the better sensor sensitivity could be obtained with high optical power of the light source, a low attenuation coefficient, and a high transmission loss difference. In Eq. (7), the term of $\Delta\alpha/\alpha_0$ is only determined by the features of the slot waveguide. Thus, we will first focus on optimizing the transverse structural parameters of the slot waveguide to achieve maximum $\Delta\alpha/\alpha_0$ and then evaluate the final performance of our proposed RI-EFA sensor with other parameters.

For practical biological and chemical sensors, the detection limit (DL) is another important criterion to evaluate the sensing performance of a RI sensor, which is defined as the detectable minimum RI variation and determined by [13]

$$\mathrm{DL} = R/S, \tag{8}$$

where R and S are the minimum detectable power of the PD (power unit, e.g., nW) and the sensor sensitivity (e.g., nW/RIU), respectively. From Eq. (8), it is obvious that better performance could be obtained by the higher sensor sensitivity and lower minimum detectable power of the PD. It should be mentioned that the minimum detectable power of the PD is power dependent in principle since the shot noise in the PD depends on the incident optical power. The detailed noise analysis and a discussion of a representative PD (Thorlabs FDS100) operating at a specific wavelength are presented in Appendix A. As discussed in Appendix A, when the output power of the light source is not so high (<1 mW), the thermal noise is dominant

in the PD. Since the optical power of an integrated system is normally less than 1 mW so that minimum detectable power of the PD could be treated as a single power-independent value at a certain operating wavelength. Specifically, the minimum detectable power is considered as $R = 2.56$ nw at 1064 nm.

3. NUMERICAL SIMULATION RESULTS

In this section, the performance of our proposed RI-EFA sensor is discussed with numerical simulations. For both of the two sensing mechanisms, the waveguide structure is first optimized by the finite element method (FEM) and the impact of different structural parameters on sensor performance is discussed. Then, with the optimized structure, the detector sensitivity is calculated. Finally, considering the interface roughness of the etched sidewalls and the length of the waveguide, the achievable DL of our proposed RI-EFA sensor is calculated and discussed.

A. Calculation for Homogeneous Sensing

1. Optimization of the Transverse Structure

The structure of the slot waveguide is shown in Fig. 1. Following our previous work [19], the height of the silicon strip is set as $h = 220$ nm, according to the standard SOI wafer, and two parameters of the total waveguide width $w_{\text{total}} = 2w_{\text{st}} + w_{\text{sl}}$ and duty cycle $\eta = w_{\text{sl}}/w_{\text{total}}$ are adopted to describe the transverse structure, where w_{st} and w_{sl} are the widths of the silicon strips and the slot as denoted in Fig. 1, respectively. According to Section 2.B, within the silicon high absorption band, the material absorption contrast between silicon and water is considerable, which is very helpful to translate the variation of light field distribution within silicon and water to a varied attenuation coefficient. Here, as a concrete example, the sensing material covered on the slot waveguide is considered as a water–isopropanol solution and the designed sensor is considered as operating at a wavelength of 1064 nm, according to our previous work and available experimental condition.

At a wavelength of 1064 nm, the RI of silicon, silicon dioxide, and water are approximated as $n_{\text{si}} = 3.5$ [22], $n_{\text{sio2}} = 1.45$ [23], and $n_{\text{water}} = 1.33$ [24], respectively. Meanwhile, the refractive index of the water–isopropanol solution will change from 1.326 to 1.370 when the concentration of isopropanol (IPA) increased from 0% (water) to 100% (pure IPA) [24,25]. In the FEM simulation, the electromagnetic field has been calculated within space coordinates of 25 μm × 25 μm. Only the quasi-TE slot mode is calculated due to stronger light confinement within the slot and cover medium region and lower transmission loss [11,19]. At the same time, the effective refractive index (n_{eff}) of propagation modes could be elaborately controlled by engineering both w_{total} and η. The details about calculating the effective RI can be found in our previous work [19]. Intuitively, for any w_{total}, as η increases, the attenuation coefficient of the slot waveguide would decrease with the reduced silicon region since the silica and water almost do not absorb the electromagnetic wave of $\lambda = 1064$ nm. Simultaneously, the effective RI decreases with the reduced silicon region. Moreover, it should be mentioned that n_{eff} should be larger than the light line (n_{sio2}); otherwise, the propagation mode would transfer to a radiation mode. Furthermore, when the RI of the cover material increases, the effective RI of the slot waveguide will also increase. In other words, the effective RI of the slot waveguide is positively correlated to the RI of the cover material. Thus, for our RI sensing, the structural parameters of the slot waveguide should ensure that n_{eff} is above the light line while the cover material is considered as water (low RI), and the detailed discussions about the mode property of slot the waveguide can be found in [19].

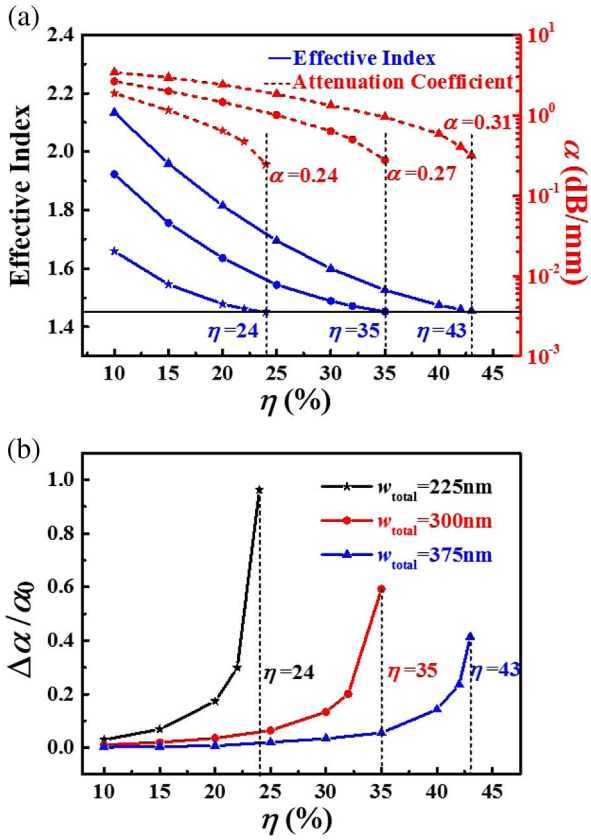

Fig. 3. (a) Calculated attenuation coefficient (red), effective RI (blue), and (b) corresponding parameter of $\Delta\alpha/\alpha_0$ with varying η of different values of w_{total}. The stars, circles, and triangles present the calculation results for total widths of $w_{\text{total}} = 225$ nm, $w_{\text{total}} = 300$ nm, and $w_{\text{total}} = 375$ nm, respectively.

Figure 3(a) shows the calculated results of the attenuation coefficient (red) and effective RI (blue) versus the duty cycle. It can be found that the effective RI of the slot waveguide will be lower than that of silica when η exceeds a certain value. Specifically, the value is $\eta = 35\%$ for the case of $w_{\text{total}} = 300$ nm, where the corresponding slot width w_{sl} is 105 nm. Figure 3(b) shows the calculated results of the parameter of $\Delta\alpha/\alpha_0$ versus the duty cycle. It could be found that $\Delta\alpha/\alpha_0$ would increase with η. Thus, there is a maximum $\Delta\alpha/\alpha_0$, according to maximum η. As shown in Eq. (7), the maximum $\Delta\alpha/\alpha_0$ is related to the best sensor sensitivity. Meanwhile, as shown in Fig. 3(a), the lowest transmission loss is also achieved. The maximum η and $\Delta\alpha/\alpha_0$ as well as the corresponding attenuation coefficient are summarized in Table 1 for $w_{\text{total}} = 225$, 300, 375 nm, respectively.

Table 1. Maximum η and $\Delta\alpha/\alpha_0$ and the Corresponding Attenuation Coefficients for Homogeneous Sensing of the Water–Isopropanol Solution

W_{total} (nm)	Max η (%)	Min α_0 (dB/mm)	Max $\Delta\alpha/\alpha_0$
225	24	0.24	0.96
300	**35**	**0.27**	**0.59**
375	43	0.31	0.41

As discussed above, for any w_{total}, there is a maximum value of η that would provide the lowest transmission loss and the highest sensor sensitivity (S) at the same time. Thus, it provides a useful guideline for optimizing the slot waveguides. However, considering the fabrication process of a practical device, we choose the parameters of $w_{\text{total}} = 300$ nm and $\eta = 35\%$ as the preferred structure in this work. Actually, the corresponding widths of the silicon strip and the slot are $w_{\text{st}} = 105$ nm and $w_{\text{sl}} = 98$ nm, respectively. They are very close and around 100 nm so that they could be readily fabricated with current nanofabrication technology.

After the transverse structure of the slot waveguide is determined, we have calculated the transmission loss of the slot waveguide while the RI of the water–isopropanol solution changes from 1.326 to 1.370. The results are summarized in Figs. 4(a) and 4(b). From Fig. 4(a), it could be seen that the attenuation coefficient would increase along with n. In detail, when the concentration of IPA (RI of water–isopropanol solution) increased, the effective RI of the slot waveguide would increase from 1.452 to 1.480 as well as the attenuation coefficient would increase from 0.27 to 0.44 dB/mm. In fact, such variation is introduced by the varied electromagnetic field distribution within the slot waveguide due to RI variation. From the inset picture in Fig. 4(a), it can be clearly seen that the light field is confined within the narrow slot region so that the field distribution is rather sensitive to both the geometric structure and the RI of the cover medium.

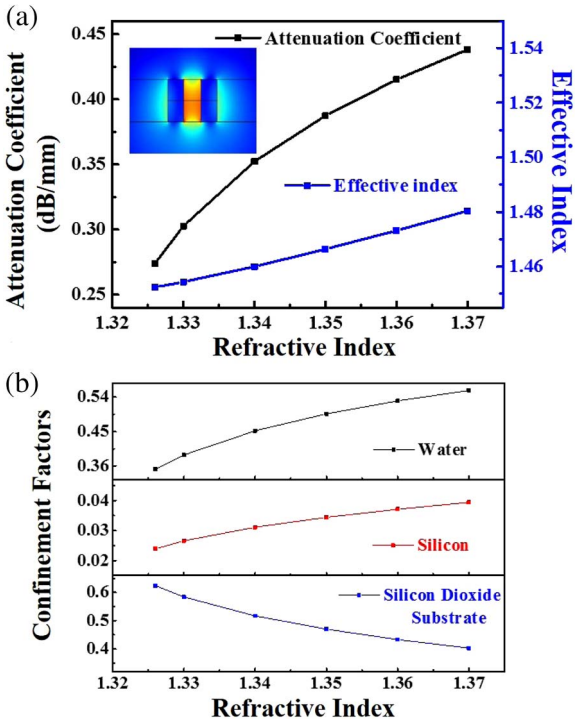

Fig. 4. (a) Calculated effective index, attenuation coefficient, and (b) corresponding confinement factor with varying RI of the IPA solution at 1064 nm with $w_{\text{total}} = 300$ nm and $\eta = 35\%$.

Moreover, the confinement factor has also been calculated with Eq. (2) through the electric field distribution. From Fig. 4(b), it can be seen that larger n means more light field enters both the silicon strip and the water cladding from that in the silicon dioxide substrate. In particular, in the silicon strip, the confinement factor is from 0.024 to 0.039. Thus, the attenuation coefficient would increase significantly.

2. Optimum Length versus Scattering Loss

As described in the previous two sections, we have been able to calculate the detection limit of our proposed RI-EFA sensor. However, the previous calculation did not consider some practical factors, such as some additional losses. In practical fabrication processes, additional losses will be inevitably introduced, including scattering loss (α_{sc}) and coupling loss between different components. Such additional loss would attenuate the optical power and thus degrade the system performance. The coupling loss extracts some extra radiation from inside the slot waveguide and could be treated as an additional attenuation term of output power. Since the coupling loss would be inversely proportional to detection limit, it only increases the power required from the light source to achieve the same detection limit.

For the scattering loss, it occurs all along the slot waveguides so that it could be treated as an additional term of the attenuation coefficient ($\alpha_{0\text{sc}} = \alpha_0 + \alpha_{\text{sc}}$), and the corresponding optimal detection limit can be calculated with Eq. (8). According to our previous work [26], the scattering loss can be simply estimated as

$$\alpha_{\text{sc}} = c \cdot \sigma^2, \tag{9}$$

where c is a coefficient related to the mode distribution of the slot waveguide. Specifically, the value is calculated as $c = 0.34$ dB/mm/nm^2 with $w_{\text{total}} = 300$ nm and $\eta = 35\%$, and the detailed discussion can be found in our previous work [26]. In Eq. (9), σ is the standard deviation of interface roughness. Following the results shown in [27], it is estimated to be $\sigma = \sim 4$ nm (the amplitude of the interface roughness is ~ 10 nm) and the scattering loss coefficient is calculated as 5.44 dB/mm. If the fabrication technologies are improved, according to reported silicon strip waveguide [27], the typical standard deviation of interface roughness can be ~ 2 nm (the amplitude of the interface roughness is ~ 5 nm) and the scattering loss coefficient in the slot would be 1.36 dB/mm. In our calculations, such two values of scattering loss are both considered. Figure 5(a) is the detection limit versus the waveguide length without scattering loss, while Fig. 5(b) shows the results with interface roughness of $\sigma = 4$ and 2 nm. Comparing Fig. 5(b) with Fig. 5(a), it is clear that less scattering loss means a higher detection limit. Specifically, the calculated highest detection limit can be 5.79×10^{-8} RIU and the corresponding optimal length is about 16.1 mm without the scattering loss. With $\sigma = 4$ and 2 nm, the detection limits are 1.24×10^{-6} and

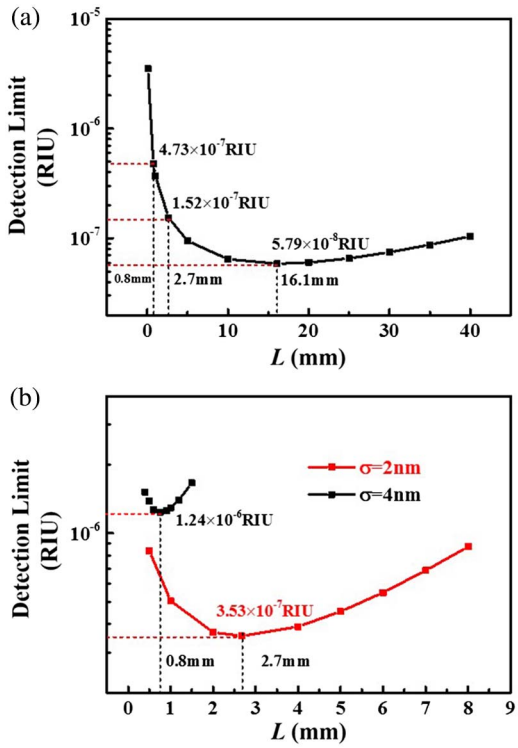

Fig. 5. (a) Detection limit versus the length of the slot waveguide for homogeneous sensing without scattering loss and (b) with different scattering losses.

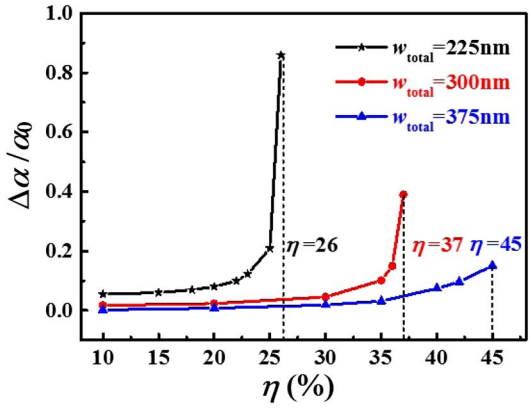

Fig. 6. Corresponding parameter of $\Delta\alpha/\alpha_0$ with varying η of different values of w_{total}. The stars, circles, and triangles present the results for total widths of $w_{\text{total}} = 225$ nm, $w_{\text{total}} = 300$ nm, and $w_{\text{total}} = 375$ nm, respectively.

Table 2. Maximum η and $\Delta\alpha/\alpha_0$ and the Corresponding Attenuation Coefficients for Surface Sensing of DNA Hybridization

W_{total} (nm)	Max η (%)	Min α_0 (dB/mm)	Max $\Delta\alpha/\alpha_0$
225	26	0.17	0.86
300	**37**	**0.20**	**0.39**
375	45	0.21	0.15

3.53×10^{-7} RIU, respectively. Furthermore, it is worth noting that although the interface roughness would affect the detection limit, a shorter optimal L of the slot waveguide could be achieved due to larger scattering loss. As shown in Fig. 5(b), the values of optimal length are 0.8 and 2.7 mm, respectively. For comparison, the detection limits at the same length of the ideal slot waveguide are also marked in Fig. 5(a) and the values are 4.73×10^{-7} and 1.52×10^{-7} RIU, which are very close to those after considering the scattering loss (1.24×10^{-6} and 3.53×10^{-7} RIU). From these results, we believe that scattering loss is not a big obstacle in achieving a RI-EFA sensor with a slot waveguide.

B. Calculation for Surface Sensing

For surface sensing, the surface of the slot waveguide is covered with a sensing material, as shown in Fig. 1(b), and the sensing material is pretreated as the receptors or binding sites, which is adhered to the surface on the silicon strips of the slot waveguide. The refractive index of this surface sensing layer would change when the receptors or the binding sites bind the specific analyte selectively. Here, the sensing function is considered to detect DNA hybridization, which is the process of two single-stranded DNA (ssDNA) combined to double-stranded DNA (dsDNA) and the corresponding refractive index (n_d) would change from 1.456 to 1.53 [28,29]. As usual, the ssDNA is considered as initially attached on the surface of the linker that is immobilized on the top of the silicon strip, and the thickness of the DNA would remain constant after the hybridization happened [28,29]. As with the calculation for homogeneous sensing, we have optimized the waveguide structure and then the achievable DL after considering the length of the waveguide. The detailed calculation results are plotted in Fig. 6 and summarized in Table 2.

Similar to homogeneous sensing, parameters of $w_{\text{total}} = 300$ nm and $\eta = 37\%$ are selected as the preferred structure and the corresponding widths of the silicon strip and the slot are $w_{\text{st}} = 95$ nm and $w_{\text{sl}} = 110$ nm, respectively. The calculated detection limit without the scattering loss is shown in Fig. 7, and the best value is DL $= 3.05 \times 10^{-7}$ RIU with corresponding optimal length of ~22.2 mm. These values are slightly inferior to those in the homogeneous sensing. For the homogeneous sensing, the RI is from 1.326 (water) to

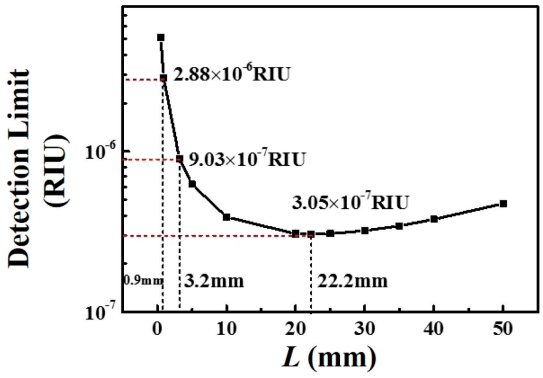

Fig. 7. Detection limit versus the length of the slot waveguide for surface sensing.

1.370 (IPA), while it is from 1.456 (ssDNA) to 1.53 (dsDNA) for surface sensing. Although the RI variation for homogeneous sensing is comparatively smaller than that for surface sensing, the transmission loss changes more since the sensing material is the entire cover medium, while there is only a thin layer of sensing material for surface sensing. Thus, our proposed RI-EFA sensor is more suitable for homogeneous sensing.

4. CONCLUSIONS

In this work, we have proposed a systematic investigation of a RI-EFA sensor based on a silicon slot waveguide for both homogenous sensing and surface sensing. The proposed sensor is considered as operating at 1064 nm, and the detection limit could be as good as $\sim 10^{-8}$ RIU for homogeneous sensing and $\sim 10^{-7}$ RIU for surface sensing with the optimized structure of the slot waveguide. Since only the straight waveguide and optical power detection are required to achieve high-performance RI sensing, the proposed architecture is very simple and promising to realize an integrated sensor on a single chip. Moreover, it could be achieved in an all silicon configuration, which would be helpful to considerably decrease the cost of a lab-on-a-chip system. We believe that our proposal has potential to achieve portable sensing devices in the future.

APPENDIX A: NOISE ANALYSIS FOR A PD

In this work, there are two kinds of noise considered, which are thermal noise (N_t) and shot noise (N_s), respectively, and they could be expressed as [30]

$$N_t = 4k_B T \cdot \Delta B \tag{A1}$$

and

$$N_s = 2(I_d + I_c) \cdot \Delta B \cdot q \cdot R_l, \tag{A2}$$

where k_B is the Boltzmann constant, T is temperature, ΔB is noise bandwidth, I_d and I_c are dark current and signal-induced current, respectively, q is the electron unit, and R_l refers to the matched load resistance. It should be noted that while discussing the detection limit case, where only a tiny variation of n occurs, the transmitted optical power variation caused by Δn is considerably small so that it could be treated as a perturbation of the total transmitted power. Therefore, at the PD port, the incident light power could be separated into two parts: a bias background power, noted as P_{bg}, and a fluctuation signal power to be detected, noted as P_s. Considering the power inject into the detector, which we choose as a small value, the relation between them could be described as $P_{\mathrm{PD}}^{\mathrm{in}} = P_{\mathrm{bg}} - P_s$ so that the signal-induced current could be expressed as

$$I_c = R_r(P_{\mathrm{bg}} - P_s), \tag{A3}$$

where R_r refers to the responsivity of the PD. In this case, where the SNR equals 1, which means the signal power and the noise power are equal [30], we could have

$$P_{\mathrm{DL}}^2 R_r^2 R_l = N_t + N_s. \tag{A4}$$

According to Eqs. (A1) and (A2) and the criteria of the PD's detection limit, by substituting Eq. (A3) into Eq. (A4), we could get a quadratic equation on P_{DL}:

$$P_{\mathrm{DL}}^2 R_r^2 R_l + 2P_{\mathrm{DL}} R_r q R_l \Delta B - [4k_B T + 2(I_d + R_r P_{\mathrm{bg}}) q R_l] \Delta B = 0, \tag{A5}$$

where P_{DL} is the minimum detectable power out of the background power (the detection limit of the PD).

In this paper, the PD is considered as the Thorlabs FDS100 (silicon PD) operating in the wavelength band of 900–1100 nm [31]. The spectral responses of the PD are shown in Fig. 8(a). In addition, T is taken as 300 K, and ΔB is taken as 1.6 kHz, according to the recommended noise filtering circuit. The solution of Eq. (A5) for a PD working at 1064 nm is shown in Fig. 8(b). According to Fig. 8(b), the detection limit of a PD versus background power could be separated into two segments. When the background power is relatively low (<1 mW), thermal noise is dominant over shot noise (denoted as segment I). As the thermal noise is independent of input power, the detection limit of the PD is nearly constant in segment I. Our calculations and discussions presented in the main text are within this segment. However, as the background power increases more, the shot noise is more and more significant. Thus, when the incident light power of the PD is more than ~1 mW, the detection limit of the PD (or R) should be treated as a function of the incident power. Such a segment is denoted as segment II, in which the performance of the PD would deteriorate with growing background power. Quantitatively speaking, within segment I, the term of $2(I_d + R_r P_{\mathrm{bg}}) q R_l$ could be omitted from Eq. (A5). Thus, the detection limit of the PD could be simplified as

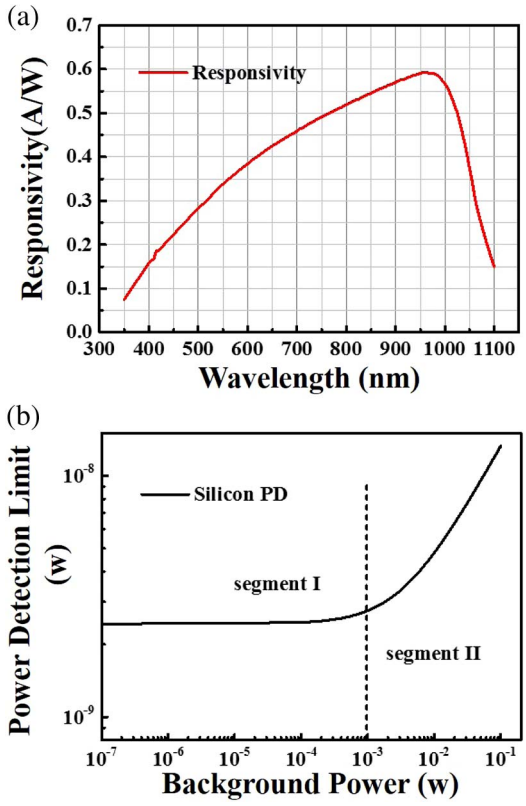

Fig. 8. (a) Spectral response of the Thorlabs FDS100 (responsivity at 1064 nm: 0.30 A/W). (b) Calculated detection limits of the silicon PD at 1064 nm versus varied background power.

$$P_{\mathrm{DL},I} = \frac{-qR_l\Delta B + \sqrt{q^2R_l^2\Delta B^2 + 4R_l k_B T\Delta B}}{R_r R_l}. \quad \textbf{(A6)}$$

Thus, in segment I, the detection limit of the PD is independent of the background power (or input power). Furthermore, according to the specific values of variables adopted in this paper, Eq. (A6) could be further simplified as $\sqrt{4R_l k_B T\Delta B}/R_r R_l$ and the resolution value in Section 2 is obtained.

For segment II, the term of $4k_B T$ could be omitted and the term of $R_r P_{bg}$ would be $R_r P_{\mathrm{bg}} \gg I_d$ with large P_{bg}. Therefore, the detection limit of the PD could be modified as

$$P_{\mathrm{DL},II} = \frac{-qR_l\Delta B + \sqrt{q^2R_l^2\Delta B^2 + 2qR_l^2R_r P_{\mathrm{bg}}\Delta B}}{R_r R_l}. \quad \textbf{(A7)}$$

Similarly, according to the specific values, the expression could be simplified as $\sqrt{2qR_r P_{\mathrm{bg}}\Delta B}/R_r$. Thus, within segment II, the detection limit of PD(R) would deteriorate with a rate proportional to $\sqrt{P_{\mathrm{bg}}}$, approximately equaling $\sqrt{P_{\mathrm{PD}}^{\mathrm{in}}}$. However, in spite of the worse resolution, the detection limit of the RI-EFA sensor will still benefit from a higher power level, according to Eq. (7). Within segment II, the detection limit will decrease with a rate of $1/\sqrt{P_{\mathrm{PD}}^{\mathrm{in}}}$ instead of $1/P_{\mathrm{PD}}^{\mathrm{in}}$.

Funding. National Science Foundation (NSF) (61621064, 61675112); National Basic Research Program of China (2013CB328704, 2013CBA01704).

Acknowledgment. The authors would like to thank Dr. Xiangdong Li and Mr. Yihang Li for their valuable discussions and helpful comments.

REFERENCES

1. T. Vo-Dinh and B. Cullum, "Biosensors and biochips: advances in biological and medical diagnostics," Fresenius J. Anal. Chem. **366**, 540–551 (2000).
2. L. D. Mello and L. T. Kubota, "Review of the use of biosensors as analytical tools in the food and drink industries," Food Chem. **77**, 237–256 (2002).
3. S. Rodriguez-Mozaz, M. J. Lopez de Alda, and D. Barceló, "Biosensors as useful tools for environmental analysis and monitoring," Anal. Bioanal. Chem. **386**, 1025–1041 (2006).
4. K. E. Sapsford, Y. S. Shubin, J. B. Delehanty, J. P. Golden, C. R. Taitt, L. C. Shriver-Lake, and F. S. Ligler, "Fluorescence-based array biosensors for detection of biohazards," J. Appl. Microbiol. **96**, 47–58 (2004).
5. K. Schmitt, B. Schirmer, C. Hoffmann, A. Brandenburg, and P. Meyrueis, "Interferometric biosensor based on planar optical waveguide sensor chips for label-free detection of surface bound bioreactions," Biosens. Bioelectron. **22**, 2591–2597 (2007).
6. C. A. Barrios, M. J. Bañuls, V. González-Pedro, K. B. Gylfason, B. Sanchez, A. Griol, A. Maquieira, H. Sohlström, M. Holgado, and R. Casquel, "Label-free optical biosensing with slot-waveguides," Opt. Lett. **33**, 708–710 (2008).
7. C. A. Barrios, "Optical slot-waveguide based biochemical sensors," Sensors **9**, 4751–4765 (2009).
8. K. Zinoviev, L. G. Carrascosa, J. Sánchez del Río, B. Sepúlveda, C. Domínguez, and L. M. Lechuga, "Silicon photonic biosensors for lab-on-a-chip applications," Adv. Opt. Technol. **2008**, 1–6 (2008).
9. A. Densmore, D.-X. Xu, P. Waldron, S. Janz, P. Cheben, J. Lapointe, A. Delge, B. Lamontagne, J. H. Schmid, and E. Post, "A silicon-on-insulator photonic wire based evanescent field sensor," IEEE Photon. Technol. Lett. **18**, 2520–2522 (2006).
10. F. Prieto, B. Sepulveda, A. Calle, A. Llobera, C. Domínguez, A. Abad, A. Montoya, and L. M. Lechuga, "An integrated optical interferometric nanodevice based on silicon technology for biosensor applications," Nanotechnology **14**, 907–912 (2003).
11. V. R. Almeida, Q. Xu, C. A. Barrios, and M. Lipson, "Guiding and confining light in void nanostructure," Opt. Lett. **29**, 1209–1211 (2004).
12. X. Fan, I. M. White, S. I. Shopova, H. Zhu, J. D. Suter, and Y. Sun, "Sensitive optical biosensors for unlabeled targets: a review," Anal. Chim. Acta **620**, 8–26 (2008).
13. C.-Y. Chao and L. J. Guo, "Design and optimization of microring resonators in biochemical sensing applications," J. Lightwave Technol. **24**, 1395–1402 (2006).
14. J. Mayer, J. Bürck, and H.-J. Ache, "Optimisation of an integrated optical evanescent wave absorbance sensor for the determination of chlorinated hydrocarbons in water," Fresenius J. Anal. Chem. **354**, 841–847 (1996).
15. E. Ryckeboer, R. Bockstaele, M. Vanslembrouck, and R. Baets, "Glucose sensing by waveguide-based absorption spectroscopy on a silicon chip," Biomed. Opt. Express **5**, 1636–1648 (2014).
16. B. D. Gupta and C. D. Singh, "Fiber-optic evanescent field absorption sensor: a theoretical evaluation," Fiber Integr. Opt. **13**, 433–443 (1994).
17. P. H. Paul and G. Kychakoff, "Fiber-optic evanescent field absorption sensor," Appl. Phys. Lett. **51**, 12–14 (1987).
18. K. Svoboda and S. M. Block, "Biological applications of optical forces," Annu. Rev. Biophys. Biomol. Struct. **23**, 247–285 (1994).
19. X. Li, X. Feng, K. Cui, F. Liu, and Y. Huang, "Designing low transmission loss silicon slot waveguide at wavelength band of high material absorption," Opt. Commun. **306**, 131–134 (2013).
20. M. A. Green, J. Zhao, A. Wang, P. J. Reece, and M. Gal, "Efficient silicon light-emitting diodes," Nature **412**, 805–808 (2001).
21. K.-Y. Cheng, R. Anthony, U. R. Kortshagen, and R. J. Holmes, "High-efficiency silicon nanocrystal light-emitting devices," Nano Lett. **11**, 1952–1956 (2011).
22. M. A. Green and M. J. Keevers, "Optical properties of intrinsic silicon at 300 K," Prog. Photovoltaics **3**, 189–192 (1995).
23. I. H. Malitson, "Interspecimen comparison of the refractive index of fused silica," J. Opt. Soc. Am. **55**, 1205–1209 (1965).
24. G. M. Hale and M. R. Querry, "Optical constants of water in the 200-nm to 200-m wavelength region," SPIE Milest. Ser. MS **118**, 80–88 (1996).
25. E. Sani and A. Dell'Oro, "Spectral optical constants of ethanol and isopropanol from ultraviolet to far infrared," Opt. Mater. **60**, 137–141 (2016).
26. X. Li, X. Feng, X. Xiao, K. Cui, F. Liu, and Y. Huang, "Experimental demonstration of silicon slot waveguide with low transmission loss at 1064 nm," Opt. Commun. **329**, 168–172 (2014).
27. Y. Vlasov and S. McNab, "Losses in single-mode silicon-on-insulator strip waveguides and bends," Opt. Express **12**, 1622–1631 (2004).
28. T. Dar, J. Homola, B. A. Rahman, and M. Rajarajan, "Label-free slot-waveguide biosensor for the detection of DNA hybridization," Appl. Opt. **51**, 8195–8202 (2012).
29. C. Viphavakit, M. Komodromos, C. Themistos, W. S. Mohammed, K. Kalli, and B. M. Azizur Rahman, "Optimization of a horizontal slot waveguide biosensor to detect DNA hybridization," Appl. Opt. **54**, 4881–4888 (2015).
30. A. Yariv, *Optical Electronics*, 3rd ed. (Holt McDougal, 1985).
31. http://www.thorlabs.com.